LASNEX simulations of the classical and laser-driven Rayleigh-Taylor instability

Karnig O. Mikaelian
Lawrence Livermore National Laboratory, Livermore, California 94550
(Received 14 February 1990)

We present the results of two-dimensional LASNEX simulations of the classical and laser-driven Rayleigh-Taylor instability. Our growth rates and eigenmodes for classical two- and three-fluid problems agree closely with the exact analytic expressions. We illustrate in several examples how perturbations feed through from one interface to another. For targets driven by a $\frac{1}{4}$-μm laser at $I=2\times10^{14}$ W/cm^2 our growth rates are 40–80% of the classical case rates for wavelengths between 5 and 100 μm. We find that radiation transport has a stabilizing effect on the Rayleigh-Taylor instability, particularly at high intensities. A brief comparison with a laser-driven experiment is also presented.

I. INTRODUCTION

In this paper we present the results of two-dimensional LASNEX (Ref. 1) simulations of the Rayleigh-Taylor[2] (RT) instability, first in the classical case where the acceleration is provided by a pressure gradient, and second in the laser-driven case where the pressure is provided by ablation. The first case was carried out to check the performance of the code on classical two-and three-fluid problems for which exact analytic answers are well known, and to illustrate feedthrough of perturbations from one interface to another. The second case was simulated because exact results are not available and there has been some controversy[3,4] over how much the ablation process stabilizes the RT instability. The numerous checks and test problems described in this paper give us confidence in our results, which are all in the linear or weakly nonlinear regime. We find that LASNEX reproduces the correct analytic growth rates and eigenfunctions for classical linear problems, including feedthrough of perturbations from one interface to another. For laser-driven plastic targets at an intensity of 2×10^{14} W/cm^2 we find growth rates that are 40–80% of the classical case rates which is consistent with more recent calculations.[5] We have already pointed out that the analytic work on density-gradient stabilization of Emery, Dahlburg, and Gardner in Ref. 3 is in error.[6] The simulations reported here suggest that density-gradient stabilization may play a more important role at high laser intensities ($I\sim10^{15}$ W/cm^2) where the effect of radiation transport is most important and leads to longer density gradients.

At lower intensities ($I\sim10^{12}$ W/cm^2) where experimental results are available,[7] our code simulations suggest little stabilization, with the growth rates being within 90–100% of $\gamma_{\text{classical}}$. This is not consistent with the large stabilization seen in the experiments, although several caveats are given in Ref. 7 and the experimental results must be taken with caution. We present the simulation of a perturbation with a square-wave pattern as was the case in the experimental targets, and our results suggest that mass transfer, which is the hallmark of the RT instability, may be hampered in square as opposed to sinusoidal perturbations. We should also point out that other experiments are in progress[8] and that a definitive answer is not yet at hand.

In Sec. II we present our classical problems. In Sec. III we present our laser-driven problems with $I=2\times10^{14}$ W/cm^2, and in Sec. IV we consider other intensities. Concluding remarks are given in Sec. V.

II. CLASSICAL RT PROBLEMS

A. $N=2$

Two fluids of densities 1 and 10 g/cm^3, each 500 μm thick, are set in motion with a constant acceleration g directed from the lighter toward the heavier fluid. We use an ideal equation of state (EOS) with an adiabatic index of 10 to suppress compressible effects, and turn off electron and ion conduction. The acceleration is generated by a pressure gradient to give $g=100$ μm/ns^2. Sinusoidal perturbations of amplitude η and wavelength λ are initialized at the interface between the two fluids. The classical result predicts that in the linear regime ($\eta\ll\lambda$) η grows exponentially in time with a growth rate γ given by

$$\gamma_{\text{classical}}=\sqrt{2\pi Ag/\lambda}\ , \tag{1}$$

where the Atwood number $A=(\rho_{\text{heavy}}-\rho_{\text{light}})/(\rho_{\text{heavy}}+\rho_{\text{light}})=9/11$ for the nominal problem described above.

Exponential growth was seen in all cases. An example is shown in Fig. 1(a). We considered $\lambda=25$, 50, 100, and 200 μm. The corresponding classical growth rates are 4.5, 3.2, 2.3, and 1.6 ns^{-1}, respectively. The growth rates agreed with $\gamma_{\text{classical}}$ to within a few percent. The eigenmodes, i.e., perturbation amplitude versus position throughout the two fluids, also agree with the classical expression [an example is shown in Fig. 1(b)]. We checked our computed growth rates against Eq. (1) by varying A, g, and λ independently, and obtained good agreement in all cases. For example, we verified that the

time evolution of $\Delta\rho r$ for two problems, one in which g was doubled and another in which λ was halved, agreed with each other.

A large number of tests were carried out to check that *variations in parameters other than the physical parameters A, g, and λ do not affect the growth rate: (a)* increasing both densities by a factor of 2; (b) increasing or decreasing the initial amplitude η_0 by factors of 10 or 100; (c) changing the adiabatic index from its nominal value of 10 to $\frac{5}{3}$ or 20—the growth rates and eigenmodes are not affected as long as g is kept constant and no shocks are introduced; (d) simulating half of a wavelength or a full wavelength gives the same γ; (e) the same γ is obtained running LASNEX fully Lagrangian or semi-Eulerian where rezoning is done only in the transverse direction; and finally (f) the zoning has a relatively small effect on these linear RT problems —we obtained 78% of Eq. (1) with our crudest zoning (8×50 mesh lines, i.e., resolving a full wavelength by eight transverse zones and the two fluids by 25 longitudinal zones each). With the code's artificial viscosity turned off, the growth rate increased to 87% of the classical rate in this crudest zoning scheme. We obtained 96% of Eq. (1) with a 40×200 mesh, and most of the tests were carried out on a 20×100 mesh, giving 92% of the classical rate. When the two fluids are allowed to "slide" freely along their common interface,[9] the rate increases to ~100% of the classical rate.

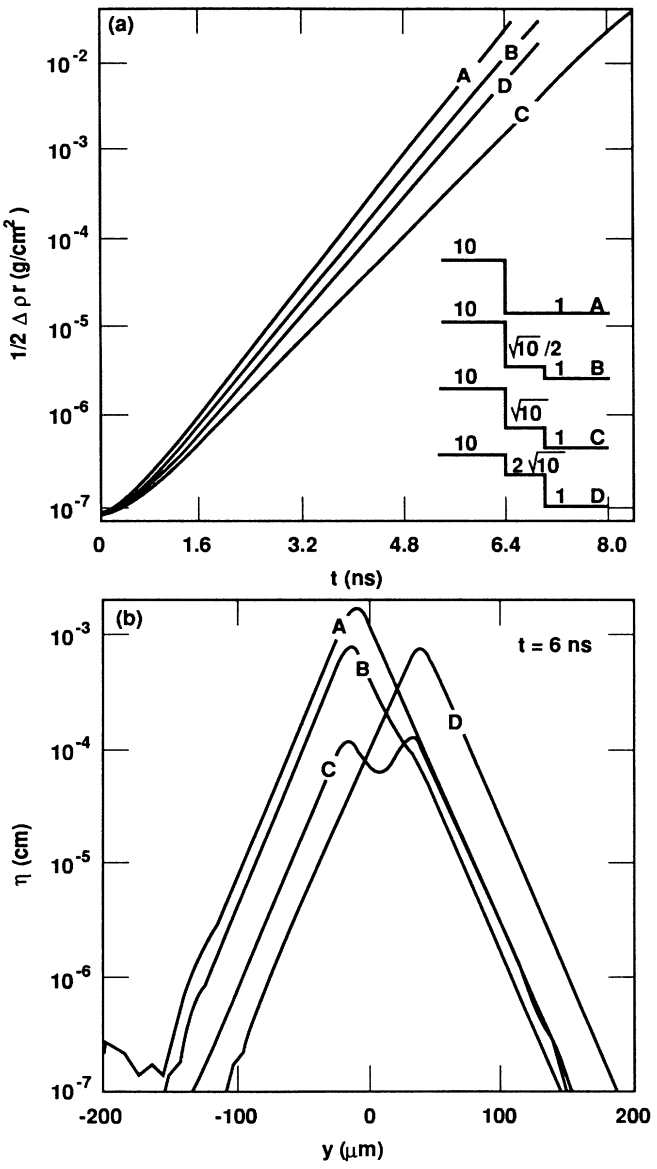

FIG. 1. (a) Evolution of $\Delta\rho r$ as a function of time for the classical two-fluid case A and three-fluid cases B, C, and D. We define $\Delta\rho r$ as the difference of $\int\rho\,dr$ taken at the maximum and the minimum of the perturbation [for two incompressible fluids $\Delta\rho r=2\eta(\rho_1-\rho_2)$]. Interfaces have initial perturbations of $\lambda=100$ μm and $\eta_0=1$ Å. (b) Perturbation amplitude vs position after 6 ns. The perturbations die off exponentially in the two outer fluids and are a linear combination of $e^{\pm ky}$ in the middle layer (Ref. 10).

B. $N=3$

Three-fluid problems were set up by "inserting" a 50-μm-thick fluid layer of density ρ_{middle} between the two original fluids. We ran most problems with perturbations of the same wavelength and amplitude at both interfaces, so that the initial $\Delta\rho r$ perturbation is the same for the two-fluid as for the three-fluid problems. In Fig. 1 we compare the two- and three-fluid problems for $\rho_{\text{middle}}=\frac{1}{2}\sqrt{10}$, $\sqrt{10}$, and $2\sqrt{10}$ g/cm^3. The two-fluid case A shown in Fig. 1 grows the fastest, and case C ($\rho_{\text{middle}}=\sqrt{10}$) grows the slowest. A few years ago we proved[10] that the growth is slowest when $\rho_{\text{middle}}=\sqrt{\rho_{\text{heavy}}\rho_{\text{light}}}$ and Fig. 1 shows that very clearly. The growth rate agrees with the analytical expressions given in Ref. 10: there are two γ's that give 1.77 and 1.84 ns^{-1} for this specific case ($g=100$ μm/ns^2, $t_{\text{middle}}=50$ μm, $\lambda=100$ μm, $\rho_1/\rho_2=\rho_2/\rho_3=1/\sqrt{10}$). LASNEX gives 1.7 ns^{-1} on a 20×112 mesh and 1.8 ns^{-1} on a 40×225 mesh. A close inspection of the eigenmodes, a snapshot of which is given in Fig. 1(b), shows how the perturbation evolves slightly faster on the lighter side even though the Atwood number is the same on both sides. This is a characteristic of the slightly faster growing eigenmode.

If we start with a perturbation at only one interface, we find that the other interface soon develops its own perturbation, which then evolves in time. This is the phenomenon of feedthrough[11] shown in Fig. 2, where we start with a perturbation only at the inner surface (between $\rho=\rho_{\text{middle}}$ and $\rho=10$ g/cm^3). The outer surface (between $\rho=\rho_{\text{middle}}$ and $\rho=1$ g/cm$_3$), which starts perfectly smooth, develops a perturbation of its own by $t\approx1$ ns that is caused by feedthrough of the perturbation from the inner to the outer surface. Conversely, perturbations can feedthrough from the outer to the inner surface also.

In Fig. 2(a) η_{outer} is always less than η_{inner} because when $\rho_{\text{middle}}=\sqrt{10}$ g/cm^3 the Atwood numbers are the same at both interfaces and η_{outer} does not overtake η_{inner}. In Fig. 2(b), where $\rho_{\text{middle}}=5$ g/cm^3, we see that η_{outer} (again induced by feedthrough) overtakes η_{inner} by $t\approx4.5$

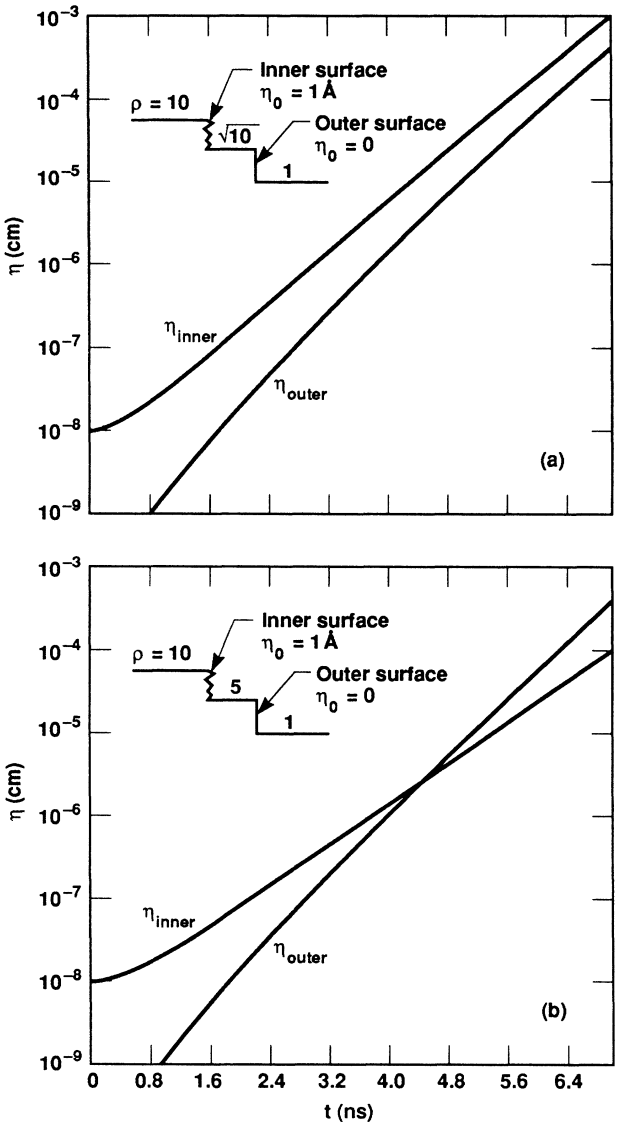

FIG. 2. Evolution of the perturbation amplitudes at the two interfaces of a three-fluid problem. Initially only one interface is perturbed with $\eta_0 = 10^{-8}$ cm. The perturbation feeds through to the other interface and grows there, faster in case (b) where $\rho_{middle} = 5$ g/cm^3.

ns. The reason clearly is that the Atwood number at the outer surface A_{outer} ($=\frac{2}{3}$) is now larger than A_{inner} ($=\frac{1}{3}$) so that the outer surface, starting with no perturbations at all, soon develops a perturbation that grows faster than η_{inner} and overtakes it. In other words, the original perturbation at the inner surface has acted as a seed for the outer surface.

III. LASER DRIVEN RT PROBLEMS

To simulate the RT instability in laser-driven targets the full machinery of the code was turned on: electron and ion conduction, laser ray trace, radiation transport, realistic EOS, etc. The target is a 25-μm-thick CH foil, driven by a $\frac{1}{4}$-μm laser with intensity increasing linearly from 0 to 2×10^{14} W/cm^2 between $t=0$ and 2 ns, and held constant thereafter. A shock wave breaks through the backside by $\sim$1 ns, after which the compressed part of the target moves at a fairly constant acceleration of about 100 μm/ns^2, the same as in our classical targets. Between $t=2$ and 5 ns perturbations are expected to grow exponentially in time. By $t\approx5$ ns the target burns through.

We initialize most of our LASNEX problems with perturbations on the backside of the target, i.e., the side away from the laser. As the shock wave breaks through, the amplitude changes phase, as expected from the Richtmyer-Meshkov (RM) instability.[12] Here we are not interested in the RM instability *per se,* but in the evolution of perturbations at the ablation front that are seeded by feedthrough from the backside to the front, much the way it happens in the RT instability as discussed above. After feedthrough the perturbation grows exponentially in time at the ablation surface, which is unstable.

Figure 3 shows a few snapshots of the computational mesh where we simulated half of a wavelength with $\lambda=20$ μm. As the perturbation grows at the ablation surface it dominates the problem and in fact feedthrough is now in the opposite direction, *from* the ablation surface *to* the backside.

It is clear from Fig. 3 that the sinusoidal form of the perturbation is maintained throughout the calculation, as expected for a linear problem. By Fourier transforming the shape of the perturbations we have tracked the evolution of the fundamental, i.e., the imposed signal at that

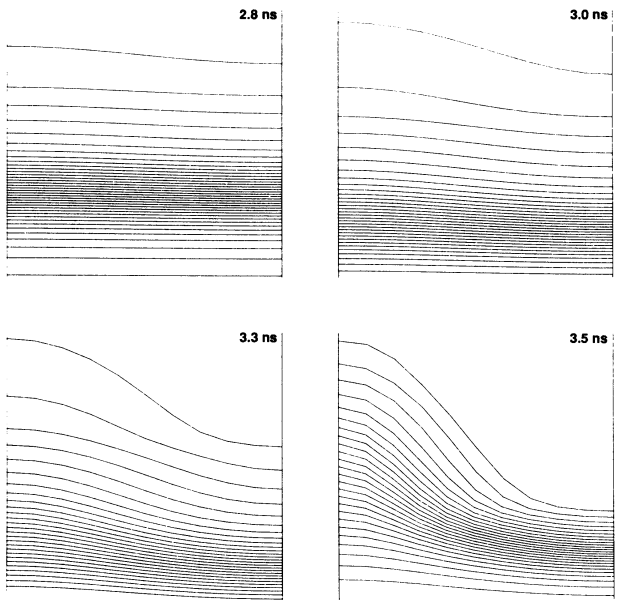

FIG. 3. Snapshots of a $\lambda=20$-μm problem at four different times. The laser is directed vertically down. The vertical (horizontal) distance is 20 μm (10 μm). Only half a wavelength is simulated. The initial amplitude was 10 Å on the backside. The final amplitude is $\sim$10 μm at the ablation surface.

specific wavelength, as well as the higher harmonics of shorter wavelength generated by and amplified in the code. We did this for both the classical and laser-driven problems. The harmonics are several orders of magnitude smaller than the fundamental, except when the problem approaches the nonlinear regime, where the wave form is expected to deviate from a sinewave and eventually develop into a bubble and a spike. Unfortunately, a fully Lagrangian or semi-Eulerian code bowties when strong shears develop in the flow, and we stop the problems at that time. (A bowtie is a quadrilateral zone in which two opposite sides intersect each other.) By initializing the problem with a small η_0 we delay bowtying so that by the time it occurs the amplitude has grown by several (typically 3–4) orders of magnitude from which a growth rate can be extracted.

In Fig. 4 we plot $\Delta\rho r$ versus time for a $\lambda=50$-μm problem with $\eta_0=100$ Å and 10 Å, confirming the expected behavior of the perturbations: $\Delta\rho r$ remains constant at its initial value of $2\eta_0\rho_{\rm CH}$ ($\rho_{\rm CH}=1$ g/cm^3) until the shock breaks through, and after $t=2$ ns, when the laser has reached full power, $\Delta\rho r$ grows exponentially in time at a rate which is independent of η_0. The third curve shown in Fig. 4 is from a problem which we ran in one dimension until $t=1.5$ ns and then linked to a two-dimensional (2D) problem with a perturbation at the ablation front near peak density. Such a comparison was made by Emery and co-workers[3] who routinely link their problems, and they obtained a rather poor agreement between these two methods. As Fig. 4 shows, a fairly unique growth rate can be extracted from our three curves: 2.7 ns^{-1}, or 77% of $\gamma_{\rm classical}$.

We can show that the exponential growth of $\Delta\rho r$ and the growth of the perturbation at the ablation surface are very closely related (experimentally, $\Delta\rho r$ is measured). Unlike the classical problems where the interface between two fluids is well defined and its distortion can be studied experimentally, the ablation surface changes continuously as the laser penetrates the target and ablates the surface (along with its deformation). To show graphically the correlation between $\Delta\rho r$ and $\eta_{\rm ablation}$, we plot in Fig. 5 $\Delta\rho r$ and $\eta_{\rm max}/\sqrt{2}$ as functions of time. $\eta_{\rm max}/\sqrt{2}$ is the largest root-mean-square variation in the surface position within the problem. Initially it is found at the backside of the target, as we mentioned above. It changes phase, as expected, when the shock wave breaks out of the backside of the target at $t\approx1$ ns, and subsequently the perturbation feeds through to the ablation surface. By $t\approx2$ ns the maximum perturbation is at the ablation surface and grows exponentially in time with a growth rate γ very close to that given by the $\Delta\rho r$ curve, viz., 2.7 ns^{-1}. Note that shock breakout reverses the phase of the amplitude at the backside (sharp dip at $t\approx0.9$ ns), but this is not enough to reverse $\Delta\rho r$, which decreases by about a factor of 2 but does not go through zero (see Fig. 5).

In addition to varying η_0 and linking (Fig. 4), we did a zoning study by doubling the number of transverse or longitudinal zones by factors of 2. We also compared Lagrangian and semi-Eulerian runs of the same problem. The growth rates agreed to within $\sim10\%$ or less.

In Fig. 6 we summarize our results for $\lambda=5$, 10, 20, 50, and 100 μm. They are, respectively, 40%, 66%, 71%, 77%, and 80% of the classical rates. The reduction from the classical rate can be described as a combination of density gradients and ablative stabilization, an example of which is shown in Fig. 6. We emphasize, however, that

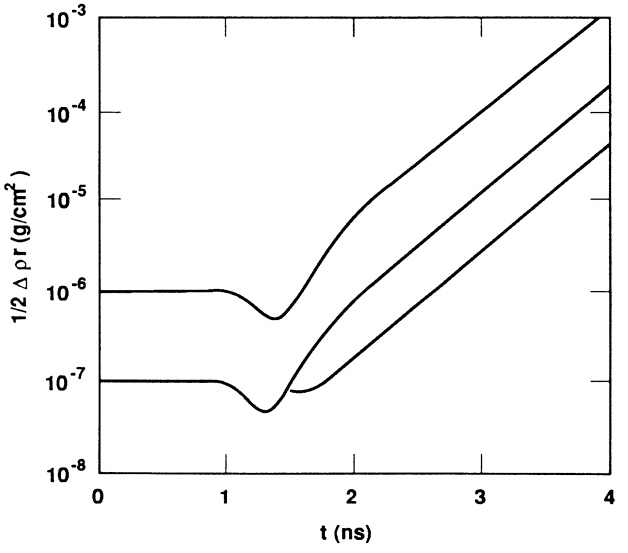

FIG. 4. Evolution of $\Delta\rho r$ as a function of time for a laser-driven problem with $\lambda=50$ μm. The two curves starting from $t=0$ had $\eta_0=10$ Å and 100 Å on the backside. These perturbations change phase when the shock breaks through. The curve starting at $t=1.5$ ns was linked from a 1D problem.

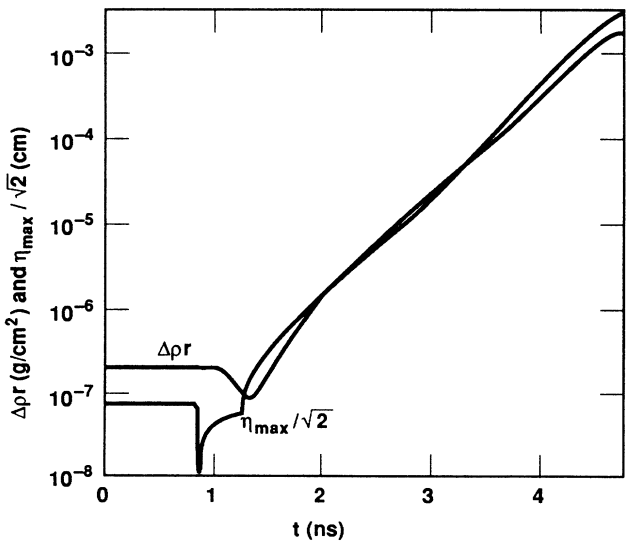

FIG. 5. Evolution of $\Delta\rho r$ and maximum root-mean-square deviation $\eta_{\rm max}/\sqrt{2}$ for a laser-driven target starting with a perturbation of $\lambda=50$ μm, $\eta_0=10$ Å on the backside. The sharp dip in amplitude signals shockwave breakout, after which the perturbation feeds through to the ablation surface and grows exponentially in time (see also Fig. 3).

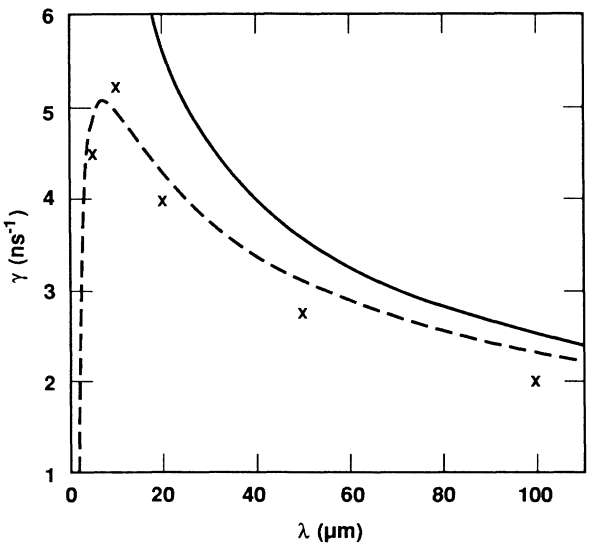

FIG. 6. γ vs λ. The LASNEX points are indicated by crosses. The continuous curve is the classical growth rate $(gk)^{1/2}$, $k=2\pi/\lambda$. The dashed curve is an approximate fit $[gk\beta/(k+\beta)]^{1/2}-Vk$ with $\beta^{-1}=1$ μm and $V=2$ μm/ns. These values are close to the density-gradient length and ablation velocity, respectively. Other fits are also possible.

such a description is not unique and our computed growth rates are not sufficient to identify the exact form of the dispersion relation—we found other fits that were equally acceptable.

In contrast to the classical problems which took less than 1 h of computing time on a CRAY-1 computer, the laser-driven problems took 4–6 h each, with 90% of the time going to radiation transport which was done by 20-group diffusion. The $\lambda=5$ μm computation was an exception in that is took 24 h because we increased the zoning to resolve such very short wavelengths and maintain a reasonable aspect ratio (~ 1) between zones. About 20 transverse zones per wavelength and 300 longitudinal zones were used. A three-temperature treatment of this problem takes only 1.5 h, but overestimates the growth rate. A three-temperature treatment appears acceptable at longer wavelengths such as 50 μm. A two-temperature treatment generally overestimates γ at practically all wavelengths though, of course, it requires the least amount of computer time.

IV. OTHER INTENSITIES

In this section we consider laser-driven problems at two other intensities: $I\sim 10^{15}$ W/cm^2 and $I\sim 10^{12}$ W/cm^2. The first was carried out to see if the stabilization improved at higher intensities (it did), and the second was carried out to see if we could explain the strong suppression or lack of growth in the experiments of Ref. 7 (we could not).

The higher intensity laser drive was patterned after the drive discussed in Sec. III, except that the peak was 10 times higher: a $\frac{1}{4}$-μm laser whose intensity increases linearly from 0 to 2×10^{15} W/cm^2, between $t=0$ and 2 ns, and is held constant thereafter. The target thickness was increased to 100 μm to prevent early burnthrough. A shock wave breaks through the backside by ~ 1 ns, after which the compressed part of the target moves at a fairly constant acceleration of about 200 μm/ns^2 (twice as large as the previous acceleration).

The 2D problems were linked from a 1D run at $t=1.5$ ns, much the way we described in Sec. III. This saved computer time and also eliminated any numerical noise associated with the (stronger) shock wave breakout.

In a preliminary run *without radiation transport* we found that the growth rates were somewhat below classical (60–80 % of classical for λ between 25 and 100 μm). A completely different picture emerged when radiation was allowed to couple to matter and was transported, again using 20-group diffusion. The early-time "growth rates" were not too dissimilar, but as the laser intensity reached its peak and stayed at 2×10^{15} W/cm^2, the growth was substantially reduced. In Fig. 7 we show the $\Delta\rho r$ evolution of the $\lambda=50$-μm perturbation with and without radiation transport. The suppression of the perturbation was even more prominent for $\lambda=25$ μm.

Since the perturbation does not grow exponentially in time, we cannot describe it with a constant rate γ (one can do so in the absence of radiation transport—see Fig. 7). Note that the acceleration of the target is fairly constant and cannot be the source for the time variation seen in γ. We believe the correct explanation is found by studying the density profiles with and without radiation transport, as we do in Fig. 8. In Fig. 8(a), without transport, the density profiles are sharp, i.e., the density gradient scales L are very small (of the order of 1 μm) and remain so through times. In Fig. 8(b), with transport, the

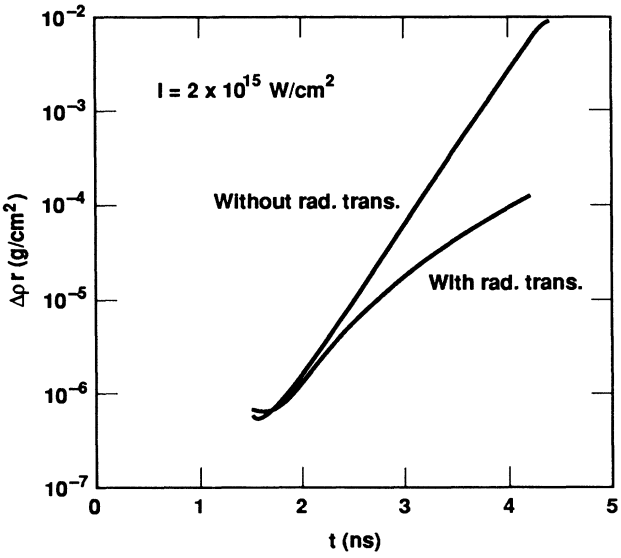

FIG. 7. Evolution of $\Delta\rho r$ for a target driven by a $\frac{1}{4}$-μm laser at $I=2\times 10^{15}$ W/cm^2, $\lambda=50$ μm, and $\eta_0=10$ Å. The two curves show the results of LASNEX simulations with and without radiation transport.

density profiles are much smoother, the density gradient scales are longer, and, perhaps more importantly, they get longer with time. This offers an explanation for the slowing down of the perturbation growth seen in Fig. 7: $L(t)$ gets longer with time.

In Ref. 6 we suggested a simplified version for density-gradient stabilization:

$$\gamma = \left[\frac{kgA\beta}{Ak+\beta} \right]^{1/2}, \tag{2}$$

where $\beta \sim 1/L$ is the inverse of the density-gradient scale length. Equation (2) is a good approximation to an exponential density profile $\rho = \rho_0 e^{\beta y}$, which can be solved exactly (see Ref. 6 for a comparison). Clearly, Eq. (2) with a time-dependent β is in good qualitative agreement with Fig. 7, and also explains why the shorter wavelength ($\lambda = 25\ \mu$m) exhibits even more stabilization.

We now turn to our lowest-intensity runs. As we mentioned earlier, these were done primarily to understand the experimental results of Grun *et al.*[7] The drive was taken to be a 1.06-μm laser pulse, Gaussian in shape with a full width at half-maximum of 4.5 ns and $I_{max} = 4 \times 10^{12}$ W/cm^2, reached at $t = 5$ ns. The targets are 10-μm-thick plastic foils. The characteristics of bulk, i.e., 1D motion, agree with the data of Ref. 7: shock breakout at $t \approx 2$ ns and peak acceleration of 8.5 μm/ns^2 at $t \approx 5$ ns.

The actual shape of the perturbation was square in the experiments. However, we first simulated a number of sinusoidal perturbations, which are the eigenmodes for the linear problems. We used $\lambda = 50-150\ \mu$m (the experimental range for square grooves) and, as usual, a variety of initial amplitudes ($\eta_0 = 10$ Å to 1 μm) to verify linearity.

We found that in all cases the growth rates are within 90–100 % of the classical rates (there is some time dependence because of the Gaussian shape of the laser pulse, hence the acceleration is not constant). These are larger than the experimental results which lie between 0 and 70% of the classical rate. Turning radiation transfer on or off in the code made little difference, as would be expected at such low intensities. Finally, we attempted the simulation of a square groove 100 μm wide and 2 μm in depth, which is shown in Fig. 9 (the perturbation was again initiated at the back side of the target). Severe bowtying after $t \approx 5$ ns, the last snapshot shown in Fig. 9, terminated this run (sinusoidal perturbations could run past 8 ns with a shape not too different from the one

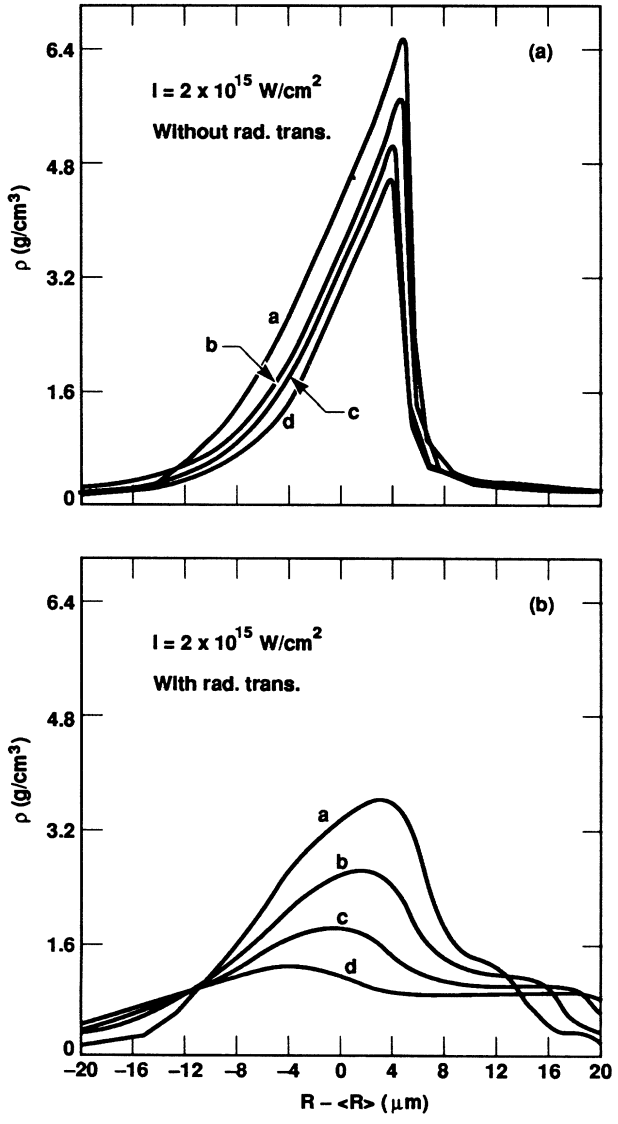

FIG. 8. Snapshots of the density profile for the simulations described in Fig. 7. Curves labeled *a*, *b*, *c*, and *d* are taken at $t = 2.5$, 3.0, 3.5, and 4.0 ns, respectively.

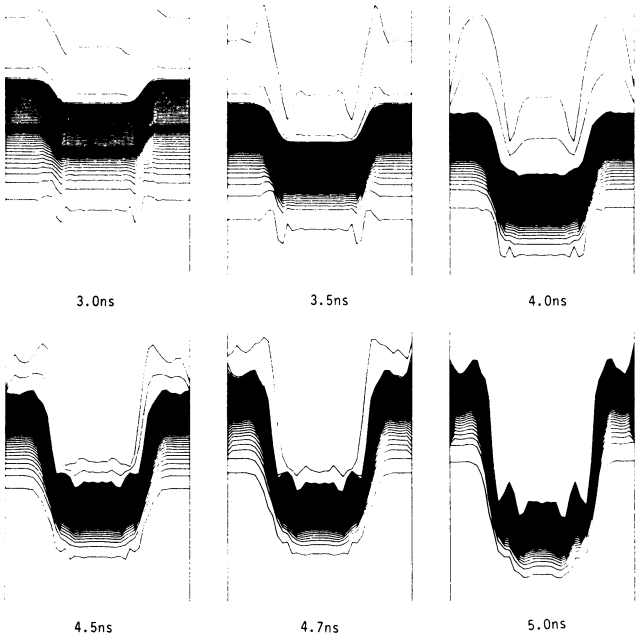

FIG. 9. Simulation of an experiment (Ref. 7) with a 2-μm-deep square perturbation on the backside of a 10-μm-thick target. The drive peaks at 5 ns. The vertical and horizontal distances are 15 and 100 μm, respectively.

shown in Fig. 3). We can, however, make some tentative conclusions based on this run. The $\Delta\rho r$ difference between the center and the edge of the groove is less than the corresponding difference in the sinusoidal case ($\Delta\rho r \sim 0.3$ mg/cm^2 by $t \sim 5$ ns), but not by much. The last snapshot in Fig. 9 suggests that mass transfer between the thick and the thin parts of the target is inhibited (compare with Fig. 3), with the sharp edge of the square acting as a bottleneck. This edge was simulated as a linear drop spread over 5μm, i.e., the target thickness varied from 9 to 11 μm over a lateral distance of 5 μm, which is probably wider than the experimental edge (a sharper edge in the simulation caused even earlier bowtying). Figure 9 suggests that, unlike a sinusoidal perturbation where mass is continually transferred from the thin to the thick part of the target, a square groove with a large initial depth (20% of the thickness in this case) causes the two parts to slide past each other without much lateral mass transfer across the sharp edge. In a sense the amplitude of the perturbation increases as the two parts separate, but without mass transfer there is little difference in $\Delta\rho r$, the experimentally measured quantity.

Simulation of such square grooves taxes the code excessively and requires numerous rezonings to continue the problem. It might be easier to carry out experiments with sinusoidal perturbations. If the lack of growth at, say, $\lambda = 50$ μm continues to hold up in sinusoidal perturbations, then we must look elsewhere for the source of that stability. Some suggestions are given in Ref. 7.

V. REMARKS AND CONCLUSIONS

The primary purpose of the research reported here was to find out if and how the RT instability at an ablating surface differs from the RT instability at a classical interface between two fluids. Our main result is given in Fig. 6, showing that the ablative growth rates are somewhat smaller than the classical rates.

All the computations reported here were done on the two-dimensional hydrocode LASNEX. To check the code an extensive series of classical tests were carried out, summarized briefly in Sec. II. Our results compared very favorably with the classical expression, Eq. (1), and we checked that spurious effects were not misleading us. Checking for zoning effects was particularly important because they would carry over to the ablative case.

In addition, we carried out a number of three-fluid simulations. Of particular importance here is the stabilizing effect of the middle layer, and the problem of feedthrough from one interface to another. The problem is not purely academic because in inertial confinement fusion (ICF) capsules the outer surface of the shell(s) may be polished off or otherwise treated for smoothness, but the inner surface(s) are not available for such post-fabrication treatment. In our classical as well as laser-driven problems we saw how perturbations feed through from the inside to the outside and seed fast-growing perturbations there.

Our ablative growth rates are only 40–80% of the classical rates, and they agree with more extensive and recent calculations,[5] but of course not with the earlier reports[3] of strongly inhibited growth (those reports were the primary motivation for undertaking this research). The implication for ICF is that shells must now be thicker than previously thought and therefore a higher energy drive is needed to implode them. The stabilizing effect of radiation coupling at high intensities (see Sec. IV) may be useful if ways can be found to increase shell density and hence its effectiveness as a tamper during the final stages of the implosion. Note that laser intensities much higher than $\sim 10^{15}$ W/cm^2 are not viable because of the various plasma instabilities that set in at higher intensities.[13] Other approaches may be found to minimize the RT instability in directly driven capsules. Needless to say, the task will be easier if the experimental results continue to show much suppressed growth, in which case we need to identify the source of such stability to take full advantage of it in ICF capsule design.

Finally, we note that new 3D codes and preliminary results in the turbulent regime have been recently reported.[14] We have presented[15] a model for turbulent energy at an ablating surface, expected to be less than the turbulent energy at a classical surface. Because of the complexity and the extensive computational time needed to perform realistic simulations, we believe that such efforts must be augmented by analytic approaches and by cross checks among codes and experiments, the ultimate purpose being to understand and predict mix and to find means of suppressing it in ICF capsules.

ACKNOWLEDGMENTS

J. Lindl suggested the study of laser-driven RT problems. I have benefited much from his suggestions and from discussions with D. Munro, M. Tabak, and G. Zimmerman. This work was performed under the auspices of the U. S. Department of Energy by the Lawrence Livermore National Laboratory under Contract No. W-7405-ENG-48.

[1]G. B. Zimmerman and W. L. Kruer, Comments Plasma Phys. Controlled Fusion **2**, 85 (1975).

[2]Lord Rayleigh, *Scientific Papers* (Dover, New York, 1965) Vol. II, p. 200; G. I. Taylor, Proc. R. Soc. London Ser. A **201**, 192 (1950).

[3]M. H. Emery, J. H. Gardner, and S. E. Bodner, Phys. Rev. Lett. **57**, 703 (1986); **62**, 694(E) (1989); M. H. Emery, J. P. Dahlburg, and J. H. Gardner, Phys. Fluids **31**, 1007 (1988); Phys. Fluids B **1**, 964(E) (1989). For a review see S. E. Bodner, M. H. Emery, and J. H. Gardner, Plasma Phys. Controlled Fusion **29**, 1333 (1987).

[4]J. D. Lindl and W. C. Mead, Phys. Rev. Lett. **34**, 1273 (1975);

J. N. Shiau, E. B. Goldman, and C. I. Weng, *ibid.* **32**, 352 (1974).

[5]J. H. Gardner, S. E. Bodner, and J. P. Dahlburg (unpublished); M. Tabak, D. H. Munro, and J. D. Lindl, Phys. Fluids B **2**, 1007 (1990).

[6]K. O. Mikaelian, Phys. Rev. A **40**, 4801 (1989).

[7]J. Grun *et al.*, Phys. Rev. Lett. **58**, 2672 (1987), and references therein.

[8]M. Desselberger *et al.*, Bull. Am. Phys. Soc. **34**, 2113 (1989); J. Grun *et al.* Bull Am. Phys. Soc. **34**, 2114 (1989).

[9]Slideline capability was recently implemented in LASNEX by G. Zimmerman.

[10]K. O. Mikaelian, Phys. Rev. Lett. **48**, 1365 (1982); Phys. Rev. A **26**, 2140 (1982).

[11]K. O. Mikaelian, Phys. Rev. A **31**, 410 (1985); **28**, 1637 (1983).

[12]R. D. Richtmyer, Commun. Pure Appl. Math. **13**, 297 (1960); E. E. Meshkov, Izv. Akad. Nauk SSSR, Mekh. Zhidk, Gaza **5**, 151 (1969); see also Ref. 11.

[13]W. L. Kruer, *The Physics of Laser Plasma Interactions* (Addison-Wesley, Redwood City, 1988).

[14]J. P. Dahlburg, J. H. Gardner, and G. D. Doolen, Bull Am. Phys. Soc. **34**, 2114 (1989).

[15]K. O. Mikaelian, J. Appl. Phys. **65**, 964 (1989).